nature communications

Article

https://doi.org/10.1038/s41467-024-55411-7

# Compositionally-graded ferroelectric thin films by solution epitaxy produce excellent dielectric stability

Received: 15 July 2024

Accepted: 11 December 2024

**Ruian Zhang**[1,12], **Chen Lin**[1,2,12], **Hongliang Dong**[3,12], **Haojie Han**[4], **Yu Song**[5,6], **Yiran Sun**[1], **Yue Wang**[4], **Zijun Zhang**[7], **Xiaohe Miao**[8], **Yongjun Wu**[1], **Zhe Ren**[9], **Qiaoshi Zeng**[3,10] ✉, **Houbing Huang**[5,6], **Jing Ma**[4], **He Tian**[1,7] ✉, **Zhaohui Ren**[1,11] ✉ & **Gaorong Han**[1] ✉

The composition in ferroelectric oxide films is decisive for optimizing properties and device performances. Controlling a composition distribution in these films by a facile approach is thus highly desired. In this work, we report a solution epitaxy of $PbZr_xTi_{1-x}O_3$ films with a continuous gradient of Zr concentration, realized by a competitive growth at ~220 °C. These intriguing films demonstrate a frequency-independent of dielectric permittivity below 100 kHz from room-temperature to 280 °C. In particular, the permittivity of the films can be largely regulated from 100 to 50 by slightly varying Zr compositional gradient. These results were revealed to arise from a built-in electric field within the films due to a coupling between the composition gradient and unidirectional spontaneous polarization. Our findings may pave a way to prepare compositionally-graded ferroelectric films by a solution approach, which is promising for practical dielectric, pyroelectric and photoelectric technical applications.

Ferroelectric materials, characterized by switchable spontaneous polarization, have been extensively explored for versatile applications in high-density memory, transducers, and sensors[1–6]. For many decades, chemical composition design, including doping or solid solution, has been an irreplaceable approach to regulating microstructure and physical properties of ferroelectric films[3], ceramics[5], and single crystals[6]. In particular, introducing a composition gradient to ferroelectrics allows the realized built-in electric field, dielectric stability[7], enhanced piezoelectricity[8], pyroelectricity[9], and geometric frustration[10], further enhancing the functionality from vibrational energy harvesting to thermal energy conversion[2]. These properties have been discussed in theory to arise from a polarization gradient ($\nabla P$) that is generated by a coupling between the composition gradient ($\nabla c$) and spontaneous polarization ($P$)[11,12].

---

[1]State Key Laboratory of Silicon and Advanced Semiconductor Materials, School of Materials Science and Engineering, Zhejiang University, Hangzhou 310027, China. [2]Key Laboratory of Intelligent Sensing Materials and Chip Integration Technology of Zhejiang Province, Hangzhou Innovation Institute of Beihang University, Hangzhou 310051, China. [3]Center for High Pressure Science and Technology Advanced Research, Shanghai 201203, China. [4]State Key Lab of New Ceramics and Fine Processing, School of Materials Science and Engineering, Tsinghua University, Beijing 100084, China. [5]School of Materials Science and Engineering, Beijing Institute of Technology, Beijing 100081, China. [6]Advanced Research Institute of Multidisciplinary Science, Beijing Institute of Technology, Beijing 100081, China. [7]Center of Electron Microscopy, School of Materials Science and Engineering, Zhejiang University, Hangzhou 310027, China. [8]Instrumentation and Service Center for Physical Sciences, Westlake University, Hangzhou 310024, China. [9]Multi-discipline Research Center, Institute of High Energy Physics, Chinese Academy of Sciences, Beijing 100049, China. [10]Shanghai Key Laboratory of Material Frontiers Research in Extreme Environments (MFree), Institute for Shanghai Advanced Research in Physical Sciences (SHARPS), Shanghai 201203, China. [11]Shanxi-Zheda Institute of Advanced Materials and Chemical Engineering, Taiyuan 030024, China. [12]These authors contributed equally: Ruian Zhang, Chen Lin, Hongliang Dong. ✉e-mail: zengqs@hpstar.ac.cn; hetian@zju.edu.cn; renzh@zju.edu.cn; hgr@zju.edu.cn

More interestingly, composition gradient ferroelectric films with a single domain have been predicted to be crucial for understanding the above intriguing properties. To realize the polarization gradient, different approaches, including metalorganic decomposition, pulsed laser deposition, and tape casting, have been employed to fabricate compositionally-graded ferroelectric thin films and multilayer composites, such as $KTa_{1-x}Nb_xO_3$[13], $PbZr_xTi_{1-x}O_3$[7,14,15], $Ba_{1-x}Sr_xTiO_3$[16], and $K_xNa_{1-x}NbO_3$[17] systems. For these emerging systems, complex component design and high-temperature (600–850 °C) crystallization are necessary, resulting in multidomain films or polycrystalline products. Moreover, component evaporation or interdiffusion at high temperatures inevitably occurs, and the ability to produce a controlled composition gradient remains a big challenge. It is thus highly desired to develop a new approach to facilely producing graded ferroelectrics by a dedicated component control at a low temperature.

In this work, we propose that a synergistic effect of competitive growth and interface polarization screening can drive the solution epitaxial growth of compositionally-graded $PbZr_xTi_{1-x}O_3$ (PZT) films. A low-temperature (~220 °C, much lower than the $T_C$ of all compositions of PZT) solution epitaxy of tetragonal single-crystal (001)-oriented PZT films on cubic (100)-oriented Nb-doped $SrTiO_3$ (Nb: STO) substrates, characterized by a compositionally-graded structure in perovskite *B*-site (Zr/Ti molar ratio) and a single-domain structure. Meanwhile, a competitive growth between the homogeneous PZT particles and the heteroepitaxial PZT films on the substrates can presumably account for the composition gradient of the films during solution epitaxy. These compositionally-graded and single-domain PZT films have been characterized to adopt a polarization gradient and thus a built-in field where a stable dielectric constant can be obtained, much lower than those of single-domain non-graded $PbZr_{0.2}Ti_{0.8}O_3$ films[18] or multidomain compositionally-graded $PbZr_{0.2}Ti_{0.8}O_3$ films[19], leading to an increased pyroelectric current (~2.4 times) along with the change of gradient under near-infrared light.

## Results and discussions

We have epitaxially grown PZT films with different variants of Zr solid solubilities ($PbZr_xTi_{1-x}O_3$, $0<x \le 0.15$, Methods and Supplementary Fig. 1) on 0.7 wt% Nb: STO substrates (a single-crystal STO with Nb doping concentration of 0.7 wt% and (100) orientation, $10 \times 10 \times 0.5\ mm^3$) by hydrothermal methods, regarding $PbZr_{0.1}Ti_{0.9}O_3$ as the main research object. Scanning electron microscope (SEM) images and energy disperse spectroscopy (EDS) results reveal that the surface of PZT films is smooth and continuous (Fig. 1a), and the Zr content in films is consistent with the designed molar ratio (Supplementary Fig. 1). Cross-sectional dark-field transmission electron microscopy (DFTEM) image of PZT/Nb: STO shows a sharp interface and a flat surface (Fig. 1b). The film with a thickness of ~900 nm has been characterized to adopt a perovskite tetragonal structure (JCPDS #70-4259) by X-ray diffraction (XRD) (Supplementary Figs. 2, 3), where an epitaxial relationship can be determined to be $<001>_{PZT}//<100>_{Nb:\,STO}$. (001) orientation of the crystallographic unit cell is known for every pixel within inverse pole figures (IPF) map obtained from electron backscattered diffraction (EBSD) analysis (Fig. 1c and its inset), which supports a single-crystal character of PZT film. In addition, uniform contrast in the out-of-plane piezoelectric force microscope (PFM) image demonstrates that PZT film adopts a single-domain structure (Fig. 1d).

To understand the stability of the single-domain structure, the electron microscopic characterization of the heterostructure has been carried out. An atomic-level cross-sectional high-angle annular dark-field scanning transmission electron microscopy (HAADF-STEM) images of PZT/Nb: STO interface (Fig. 2a) and PZT surface (Fig. 2d) further identify the high-quality epitaxy of PZT films, where the Zr/Ti ions uniformly shift upwards relative to the center of the four nearest Pb ion

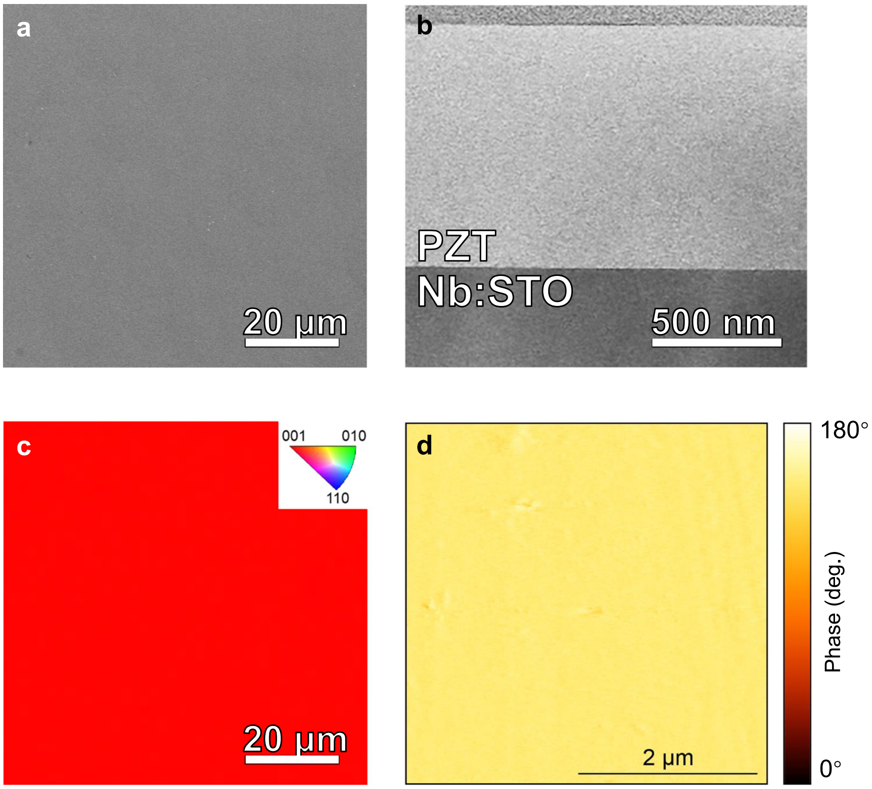

**Fig. 1 | Solution epitaxy of single-crystal and single-domain $PbZr_{0.1}Ti_{0.9}O_3$ film on Nb: STO. a** SEM image of PZT film surface. **b** Cross-sectional DFTEM image of PZT/Nb: STO. **c** EBSD IPF-Z map of PZT film surface (step size = 2 μm). The legend for interpreting the IPF map is shown in the inset. **d** Out-of-plane PFM phase image of PZT film surface.

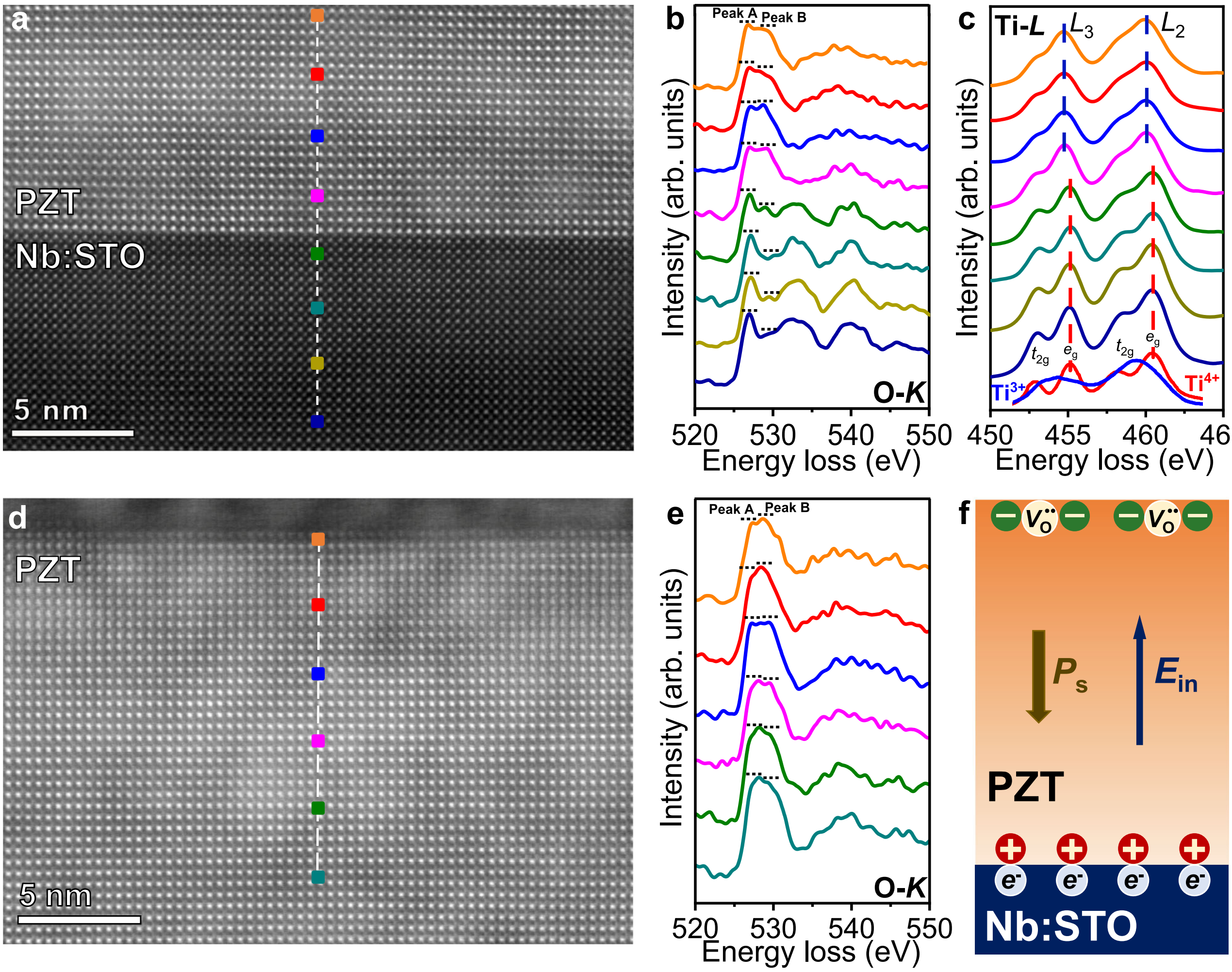

**Fig. 2 | Single-domain structure of PZT films synergistically stabilized by the oxygen vacancies at the surface and the electronic polarization screening at the interface.** **a**, **d** Atomic-level cross-sectional HAADF-STEM images of PZT/Nb: STO interface (**a**) and PZT surface (**d**). **b**, **c** A series of O-*K* (**b**) and Ti-$L_{2,3}$ (**c**) spectra across the interface from PZT to Nb: STO are plotted with colored solid lines, which were acquired from the regions with corresponding colored dots in (**a**). The reference spectra of $Ti^{3+}$ and $Ti^{4+}$ are shown at the bottom of (**c**). **e** A series of O-*K* spectra across the surface region of PZT film are plotted with colored solid lines, which were acquired from the regions with corresponding colored dots in (**d**). **f** Schematic illustration of the polarization screening of PZT film. The positive polar interface and the negative polarization surface of PZT are screened by negative charges (electrons in Nb: STO substrate) and positive charges (oxygen vacancies confined at PZT surface), respectively.

columns (Supplementary Fig. 4a–i) indicates the uniform downwards polarization[20]. Core loss spectra of electron energy-loss spectroscopy (EELS) with various colors in Fig. 2b, c, e were acquired from the regions with the corresponding colored dots in Fig. 2a and d, respectively. The relatively higher peak B compared to peak A in the upper two O-*K* spectra (Fig. 2e) reveals that large-amount oxygen vacancies[21,22] were confined at several unit cells near the PZT film surface, which gradually decreases from the surface to the inner part. The O 1*s* X-ray photoelectron spectroscopy (XPS) spectrum of PZT film further confirms that oxygen vacancies were confined near the surface (Supplementary Fig. 5). In contrast, no obvious oxygen vacancies can be detected near the interface (Fig. 2b). Meanwhile, the downwards polarization and the +4-valence state of Ti ions near the interface (Fig. 2c). According to the reference spectra of $Ti^{3+}$ and $Ti^{4+}$ at the bottom of Fig. 2c, $t_{2g}$ and $e_g$ two peaks would merge to a single peak if the Ti ions mainly exist with the +3-valence state[23]. These results argued that the electrons from *n*-type Nb: STO substrates can electrostatically screen the bound charges at the positive (001) polarization surface of PZT film, which is beneficial for lowering the interface energy and driving the solution epitaxy, like that of $PbTiO_3$ films[22,24]. Furthermore, the positively charged oxygen vacancies near the surface of the film could effectively compensate for the bound charges at the negative (001) polarization surface. Hence, the above two mechanisms are proposed in Fig. 2f to synergistically stabilize the single-domain structure of PZT films, where solution epitaxy temperature (~220 °C) is much lower than Curie temperature ($T_c$) of PZT with ferroelectric phase transition occurring.

Furthermore, it is interesting to find a smooth compositionally-graded structure (for both Zr and Ti elements) throughout the film thickness. Time-of-flight secondary ion mass spectrometry (TOF-SIMS) analysis has been conducted for the depth profiling of Zr and Ti concentrations in PZT film, revealing their composition gradient from surface to interface (Fig. 3a, Zr content gradually decreases from surface to interface and vice versa for Ti). Such a gradient distribution of the composition in the epitaxial perovskite oxide films of ferroelectrics has been investigated as the compositionally-graded ferroelectrics, which is usually obtained by vapor-phase epitaxy[7,16,19,25]. However, a single-domain film is actually quite difficult to fabricate because of the paraelectric-ferroelectric phase transition of the film during the cooling process of the vapor-phase epitaxy. As a comparison, compositionally-graded and single-domain PZT films have grown on Nb: STO substrate via such a low-temperature solution epitaxy

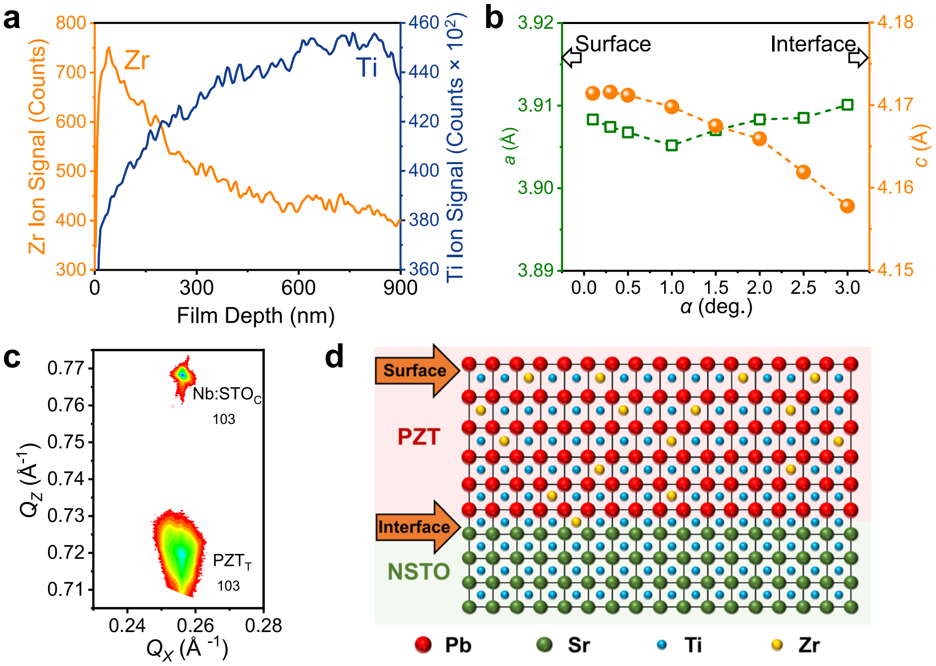

**Fig. 3 | Characterization of compositionally-graded structure in PZT epitaxial films.** **a** TOF-SIMS for the depth profiling of PZT film, implying a *B*-site compositionally-graded structure. **b** Parameters *a* and *c* as a function of the incident angle *α* of the X-ray beam determined by synchrotron-based GIWAXS. **c** Off-axis X-ray RSM study about the pseudocubic 103-diffraction condition of PZT/Nb: STO showing that the PZT film with compositionally-graded structure is coherently strained to the Nb: STO substrate. **d** Schematic of the compositionally-graded structure of PZT epitaxial film.

method. In addition, a scanning transmission electron microscopy with energy dispersive X-ray spectroscopy (STEM-EDS) has been used to detect the Zr content in the *B*-site at the interface and the surface of PZT film (Supplementary Fig. 6), where the film composition developed smoothly from nearly $PbTiO_3$ (at the interface) to nearly $PbZr_{0.2}Ti_{0.8}O_3$ (at the surface). Further, we utilized synchrotron-based grazing incident wide-angle X-ray scattering (GIWAXS) to study the thickness-dependent unit cell parameters of the PZT films. Reduced GIWAXS profiles with the various incident angle *α* shown in Supplementary Fig. 7 indicate that the d-spacing of $(112)_{PZT}$ and $(202)_{PZT}$ face monotonously decreases with *α* increasing, implying a lattice gradient. More specifically, the unit cell parameter *c* has been calculated to expand with the Zr content increasing, whereas *a* does not change significantly (Fig. 3b). Supplementary Fig. 4 shows a detailed statistical analysis of the polarization gradients within the compositionally-graded ferroelectric films. From Supplementary Fig. 4i, the out-of-plane displacements of Zr/Ti ions gradually developed from 0.079 ± 0.013 Å near the interface to 0.129 ± 0.019 Å at the surface, further supporting the downwards polarization and the existence of polarization gradient. Meanwhile, the lattice constant *c* increases from the interface (4.160 ± 0.002 Å) to the surface (4.168 ± 0.004 Å) in Supplementary Fig. 4j, whereas no obvious change in the lattice *a* can be observed. These results agree well with the results of synchrotron-based GIWAXS (Fig. 3b). Off-axis X-ray reciprocal-space mapping (RSM) about the 103-diffraction condition of PZT film and Nb: STO substrate supports that the PZT film is *c*-axis oriented without forming *a*-domains (Fig. 3c). The 103-diffraction peak of PZT film distinctly extends in $Q_z$, verifying the existence of the lattice gradient, arising from the composition gradient. Based on the above results, the compositionally-graded PZT film could be schematically described in Fig. 3d.

One should note that the formation of PZT particles is more favorable thermodynamically than the film. To understand the formation of composition gradient, a reaction time-dependent microstructure evolution of PZT films and particles has been systematically investigated (Fig. 4c–j). Energy disperse spectroscopy (EDS) by SEM analysis indicates an opposite tendency of Zr content (Zr/(Zr+Ti)) in PZT particles and films upon the reaction time prolonged (Fig. 4a), revealing a possible competitive relationship between a homogenous nucleation-growth of PZT particles and heteroepitaxy of PZT films on the substrates in solution. The epitaxial growth of PZT films appears to be suppressed during the initial stage (~3 h). In contrast, the Zr content in particles at this stage (~33%) is extremely higher than the designed molar ratio of ~10%. As the reaction time is prolonged, Zr content in the films gradually increases to ~10% after a reaction of 12 h and the corresponding one decreases in the particles. In addition, XRD patterns of PZT particles synthesized at 2, 4, 8, and 12 h (2*θ* between 20.5° and 23.5°) in Fig. 4b supports this result, where *a* and *c* of PZT particles decrease from 3.931 and 4.177 Å at 2 h to 3.921 and 4.167 Å at 8 h, respectively. Since the ionic radius of $Zr^{4+}$ (0.720 Å) is larger than that of $Ti^{4+}$ (0.605 Å)[26], the decrease of *c* during the reaction from 2 to 8 h agrees well with the gradual decrease of the Zr content in PZT particles. As discussed theoretically and experimentally, the Gibbs energy of the formation of Zr-rich PZT is lower than that of Ti-rich PZT in the Pb-Zr-Ti hydrothermal system[27] and the pure-phase $PbZr_{0.52}Ti_{0.48}O_3$ particles could be obtained in 2 h at ~200 °C[28]. Therefore, it can be inferred that the particles undergo a rapid process of homogenous nucleation to form a pure phase of PZT particles (Zr-rich PZT), where the molar ratio is much higher than the designed molar ratio of 10%. Most of Zr raw in the hydrothermal system has been consumed to form pure-phase particles, and only a few of Pb and Ti raw have been sustained in the solution at this time, which may largely limit the heteroepitaxy of PZT on the substrate. During the subsequent growth of the particles, an Ostwald ripening process drives the re-dissolution of metastable Zr-rich PZT nanoparticles. This will give rise to an increase of Zr content in solution and thus enable the heteroepitaxy of PZT. Therefore, the composition gradient can be formed in the film before the dissolution balance among the PZT particles, films, and the solution is achieved.

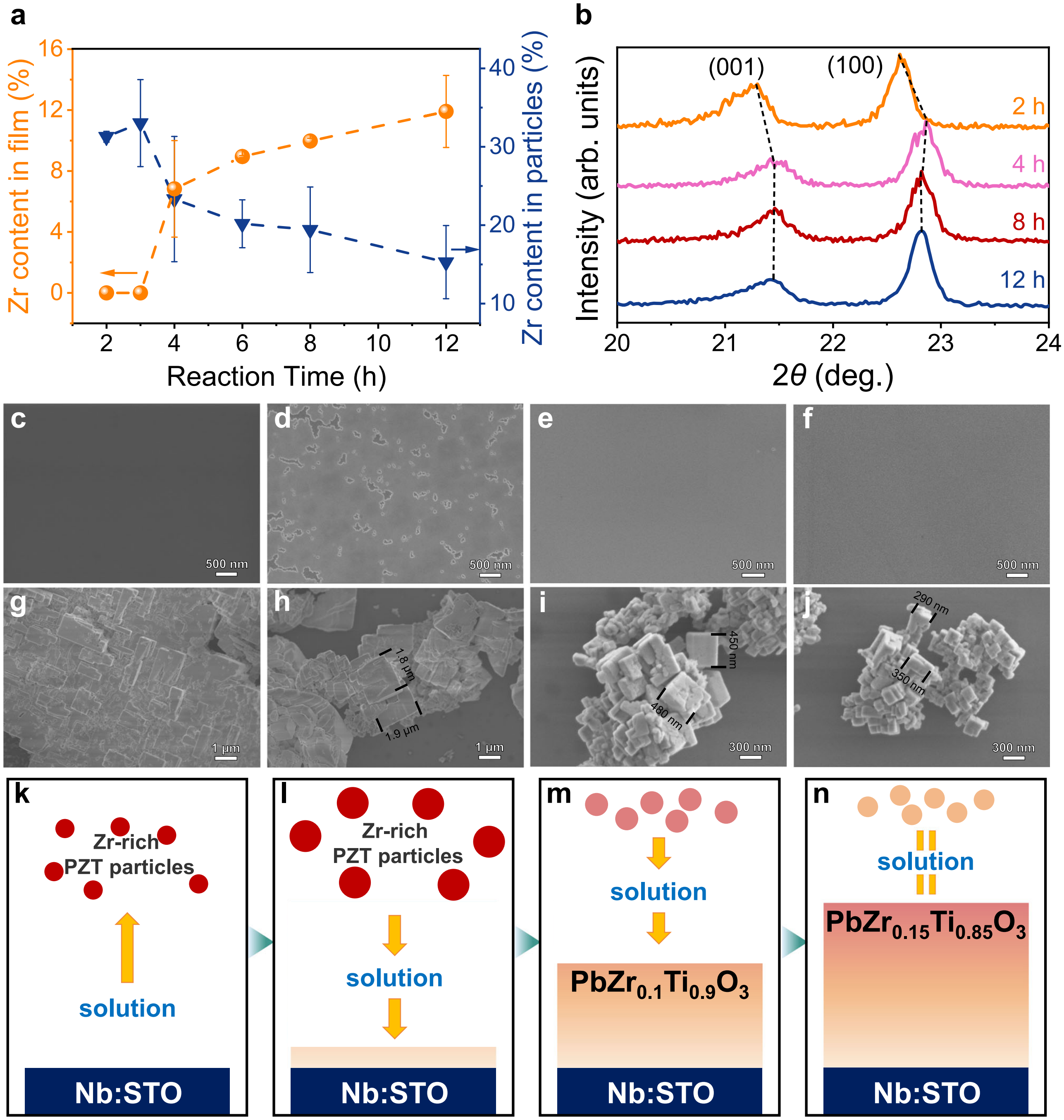

**Fig. 4 | Competitive growth kinetically driven the emergence of the compositionally-graded structure. a** Zr/(Zr + Ti) molar ratio of PZT films and particles spontaneously synthesized in the same autoclaves measured by EDS, which were synthesized for different times by hydrothermal reaction. Each error bar denotes the s.d. of the Zr/(Zr + Ti) molar ratio of three parallel samples. **b** XRD patterns of PZT particles synthesized for different times by hydrothermal reaction. **c**–**j** SEM images of PZT films and particles obtained in the same autoclaves by hydrothermal synthesis for (**c**, **g**) 2 h, (**d**, **h**) 4 h, (**e**, **i**) 6 h, (**f**, **j**) 8 h, respectively. **k**–**n** Schematic illustration of four steps of the competitive growth that kinetically drive the emergence of the compositionally-graded structure.

Herein, the Zr content in the solution as a function of the hydrothermal reaction time is simply illustrated in Supplementary Fig. 8, and the continuous variation of Zr molar ratio in solution behaved like the targets with different compositions for the vaper-phase epitaxy.

According to the above results, a growth mechanism was proposed in Fig. 4k–n, where the competition growth between the films and particles drives the appearance of compositionally-graded PZT films. At the initial stage of hydrothermal reaction, it is thermodynamically preferred that most of raw materials (especially for Zr) homogenously nucleate and grow in particles, while the nucleation and growth of epitaxial film on substrate is thus kinetically limited (Fig. 4k, first 2–3 h). As the reaction proceeded, the dissolution of particles dynamically changed the Zr/(Zr+Ti) molar ratio in solution, providing varying Zr concentration for the epitaxy, resulting in the compositionally-graded PZT film (Fig. 4l–n, 4–12 h).

It has been predicted that large built-in electric fields could be obtained in compositionally-graded ferroelectrics that give rise to a polarization gradient[29]. Accordingly, a built-in electric field has been identified in the compositionally-graded PZT films, supported by a

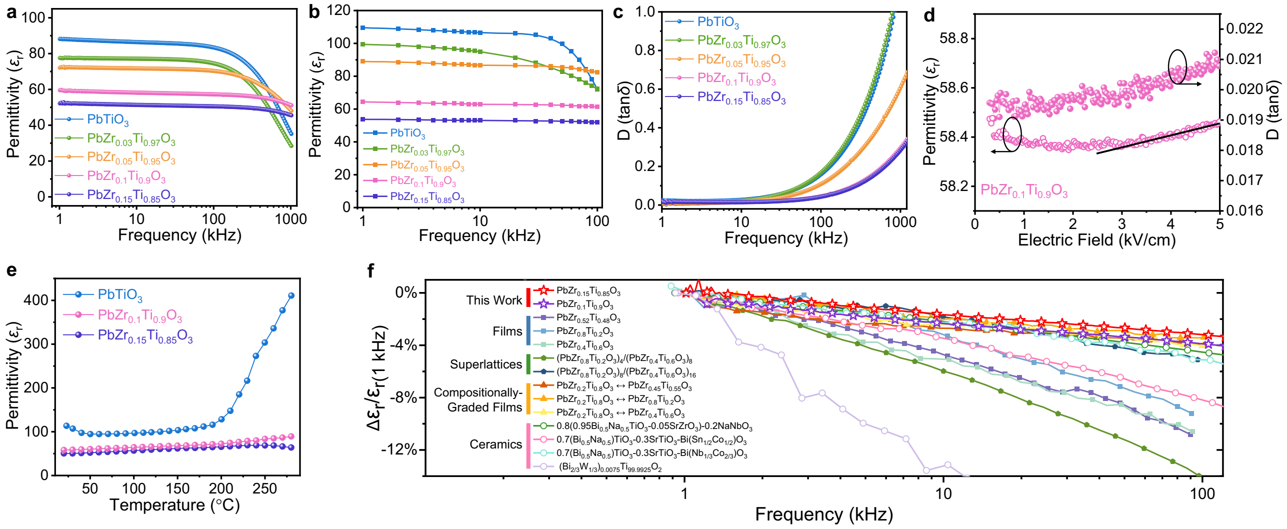

**Fig. 5 | Dielectric properties of the compositionally-graded single domain PZT film.** **a**, **c** Room temperature dielectric permittivity (**a**) and loss tangent (tan$\delta$) (**c**) as a function of frequency for PTO film and the compositionally-graded PZT (PbZr$_x$Ti$_{1-x}$O$_3$, x = 0.03, 0.05, 0.10, and 0.15) films with an ac excitation voltage of 500 mV. **b** Dielectric constant of PZT (PbZr$_x$Ti$_{1-x}$O$_3$, x = 0.0, 0.03, 0.05, 0.10, and 0.15) by phase-field method. **d** Room temperature dielectric (open data) and loss tangent (filled data) as a function of ac voltage at 10 kHz for compositionally-graded PbZr$_{0.1}$Ti$_{0.9}$O$_3$. The linear fit of the dielectric constant versus applied ac voltage using the Rayleigh law. **e** Dielectric permittivity as a function of temperature for PTO film and the compositionally-graded PZT films (PbZr$_x$Ti$_{1-x}$O$_3$, x = 0.10, and 0.15) measured with a 10 kHz ac excitation voltage of 500 mV. **f** Dielectric permittivity change in the frequency range from 1 to 100 kHz for various films and ceramics.

~1.36 V photovoltage (Supplementary Fig. 9). To determine the dielectric and pyroelectric property possibly modified by the built-in field, a sandwich structure capacitor of the films was fabricated, in which Ag electrode (area: ~0.00785 cm$^2$, thickness: ~40 nm) and 0.7 wt % Nb: STO electrode were used, respectively.

Figure 5a shows the frequency-dependent permittivity of the pure PbTiO$_3$ (PTO) film and the compositionally-graded PZT (PbZr$_x$Ti$_{1-x}$O$_3$, x = 0.03, 0.05, 0.10, and 0.15) films that have a similar thickness (Supplementary Fig. 1). Interestingly, these single-domain epitaxial films exhibit a low permittivity that gradually decreases as Zr concentration grows, and their dielectric relaxation above 100 kHz is largely suppressed, resulting in a stable permittivity (<4% change) from 1 kHz to 1 MHz for PbZr$_{0.1}$Ti$_{0.9}$O$_3$ and PbZr$_{0.15}$Ti$_{0.85}$O$_3$, agreeing with the result calculated by phase-field method in Fig. 5b. In particular, the compositionally-graded PbZr$_{0.15}$Ti$_{0.85}$O$_3$ film yields a dielectric permittivity of ~50 at 10 kHz. This value is much lower than the permittivity (~90) of single-domain PbZr$_{0.2}$Ti$_{0.8}$O$_3$ film[18]. In addition, the present permittivity is also lower when the up-graded from PbZr$_{0.2}$Ti$_{0.8}$O$_3$ to PbZr$_{0.8}$Ti$_{0.2}$O$_3$ film (~83)[7,19], in which a built-in electric field is up to ~200 kV/cm that efficiently diminishes the extrinsic contribution of the 90° domain wall. Moreover, the permittivity is quite stable in the frequency range from 1 to 100 kHz, which is superior to that of other films and ceramics, as indicated in Fig. 5f[7,30–33]. Such low and stable permittivity is probably attributed to the single-domain structure and built-in electric field that suppresses the small signal susceptibility of dipoles[16].

Correspondingly, the loss tangent (tan$\delta$) of PbZr$_{0.1}$Ti$_{0.9}$O$_3$ and PbZr$_{0.15}$Ti$_{0.85}$O$_3$ films is below 0.03 at 60 kHz (Fig. 5c). Furthermore, a detailed Rayleigh behavior investigation has been used to verify the intrinsic-extrinsic contributions to the dielectric properties of PZT films, where Rayleigh law

$$\varepsilon_r = \varepsilon_{\text{init}} + \alpha E_0 \qquad (1)$$

could greatly extract the extrinsic contribution of the dielectric permittivity[34]. The linear fitting of dielectric permittivity versus applied ac voltage at 10 kHz using the Rayleigh law, was shown in Fig. 5d (PbZr$_{0.1}$Ti$_{0.9}$O$_3$) and Supplementary Fig. 10 (PTO and PZT films). The $\varepsilon_{\text{init}}$ indicates the part of intrinsic permittivity, while the Rayleigh coefficient ($\alpha$) gives a quantitative measurement of the extrinsic contribution to the permittivity, such as the irreversible displacement of the domain walls under an external field[25]. The values of the Rayleigh coefficient for PTO, PbZr$_{0.1}$Ti$_{0.9}$O$_3$, and PbZr$_{0.15}$Ti$_{0.85}$O$_3$ are 0.006, 0.042, and 0.051, respectively, which are almost an order of magnitude smaller than the previous reports (Supplementary Table 1). This result reveals a dominant and intrinsic contribution to the low and stable permittivity. As predicted, the built-in field induced by the flexoelectric effect could diminish a temperature dependence of the polarization and susceptibility of ferroelectrics[12]. Therefore, we conducted temperature-dependent permittivity measurements on the films in Fig. 5d. It was found that PbZr$_{0.1}$Ti$_{0.9}$O$_3$ and PbZr$_{0.15}$Ti$_{0.85}$O$_3$ films yield a stable permittivity from room temperature to 280 °C owing to the composition gradient. In contrast, the permittivity of PTO abruptly increased above 200 °C, corresponding to a ferroelectric phase transition[35].

Low permittivity and high polarization are desirable for optimizing the pyroelectric effect, which can be discussed by figure of merit (FoM)

$$k^2 = \pi^2 T / C_p \varepsilon_r \varepsilon_0 \qquad (2)$$

where $\pi$ is the pyroelectric coefficient, $T$ is the temperature of operation, $C_p$ is the heat capacity, and $\varepsilon_0$ is the permittivity of free space[7,19,36]. A pyroelectric response of the films under 1064 nm near-infrared (NIR) laser irradiation has been investigated in Supplementary Fig. 11. The pyroelectric current (2.6 nA) of compositionally-graded PbZr$_{0.15}$Ti$_{0.85}$O$_3$ film is 2.4 times higher than that of pure PTO film. In addition, a steady-state short-circuit current of ~12.0 µA (1.527 mA/cm$^2$) under 375 nm irradiation has been obtained, demonstrating a quick switching-on light response (Supplementary Fig. 12). By using a dynamic method[13,37] (Methods, Supplementary Fig. 13 and Supplementary Table 2), the pyroelectric coefficients of PbZr$_{0.1}$Ti$_{0.9}$O$_3$ and PbZr$_{0.15}$Ti$_{0.85}$O$_3$ films have been determined to be −265 and −274 µC/m$^2$K, respectively. One should note that the low dielectric permittivities of the compositionally-graded $PbZr_{0.1}Ti_{0.9}O_3$ and $PbZr_{0.15}Ti_{0.85}O_3$ films allow to obtain improved figures of merit of 0.0139 and 0.0166, which are ~1.2 and ~1.5 times higher than that of compositionally up-graded $PbZr_{0.2}Ti_{0.8}O_3$ to $PbZr_{0.8}Ti_{0.2}O_3$ film[19], respectively.

In summary, the solution epitaxial growth of single-domain PZT ($PbZr_xTi_{1-x}O_3$, $0<x \le 0.15$) films with smooth composition gradients has been achieved on Nb: STO substrates. The competitive growth in a closed solution system allows for kinetically driving the composition gradient. Correspondingly, the single-domain structure of the film has been revealed to be synergistically stabilized by the oxygen vacancies on the surface and the electronic polarization screening from the substrates, yielding a uniform and downward polarization pointing to the substrates. These compositionally-graded PZT films demonstrate an extremely low dielectric permittivity (~50) with excellent frequency (1–100 kHz) and temperature (room temperature to 280 °C) stability. Due to the composition gradient, a prominent photovoltaic effect and pyroelectric current have been obtained in the ultraviolet and near-infrared range. These findings would offer the opportunity to elucidate intrinsic physic properties of the compositionally-graded ferroelectrics and make them highly attractive for dielectric, pyroelectric, and passive optoelectrical detection applications.

## Methods

### Materials

Lead nitrate ($Pb(NO_3)_2$, ≥99.0%), zirconium oxychloride octahydrate ($ZrOCl_2{\cdot}8H_2O$, ≥99.9%), tetrabutyl titanate (TBOT, ≥98.0%), potassium hydroxide (KOH, ≥85.0%), methyl cellosolve (≥99.5%), ammonium solution (the $NH_3$ content is 25–28%), acetone (≥99.5%), and ethanol (≥99.7%) were purchased from Sinopharm Chemical Reagent Co. Ltd. and used without further purification. 0.7 wt% Nb: $SrTiO_3$ (Nb: STO) single-crystal substrates with dimensions $10 \times 10 \times 0.5\ mm^3$ and (100) orientation were obtained from Shenyang Baijujie Corporation, and they were two-side polished.

### Film preparation

PZT ($PbZr_xTi_{1-x}O_3$, $0<x \le 0.15$) films were synthesized by a solution epitaxy consisting of co-precipitation and hydrothermal processes as follows: $ZrOCl_2{\cdot}8H_2O$, TBOT, and $Pb(NO_3)_2$ were used as starting materials. KOH was used as a mineralizer. Nb: STO substrates were cleaned ultrasonically with acetone, ethanol, and deionized water before use, and then they were placed in a Teflon holder for drying. Firstly, 0.03–0.08 g $ZrOCl_2{\cdot}8H_2O$, 0.75–0.98 g $Pb(NO_3)_2$, and corresponding TBOT were dissolved in methyl cellosolve to synthesize the precursor solution. Note that the Pb/(Zr + Ti) molar ratio was set as 1.2:1. Excess ammonium solution was dripped into the precursor solution to obtain the co-precipitation of Pb, Zr, and Ti. The co-precipitate was filtered out and cleaned five times with deionized water. Secondly, the co-precipitation was added to a KOH solution, the concentration of which was ~1.5 mol/L. After a 2-h continuous stirring process at room temperature, the Nb: STO substrate was placed in the solution of the autoclave in preparation for the hydrothermal treatment under 220 °C for 3–24 h. During this period, the Nb: STO substrate was held horizontally at a height of 15 mm above the bottom of the autoclave. After the hydrothermal treatment, the resulting products underwent a thorough washing process using deionized water and ethanol several times. Subsequently, they were dried in air at a temperature of 60 °C to enable further characterization.

### Characterization

The structures of the PZT/Nb: STO samples were comprehensively characterized using a variety of advanced techniques. X-ray Diffraction (XRD, Rigaku D/max-RA, Cu $K_\alpha$ radiation, $\lambda = 1.5406$ Å) was employed to analyze the crystalline structure. The surface morphology was examined by a scanning electron microscope (SEM, Hitachi SU-70) and a Scanning probe microscope (SPM, Asylum Research, Cypher S and MFP-3D). The synchrotron radiation GIWAXS measurements of PZT/Nb: STO samples were conducted at the beamline 17B1 of Shanghai synchrotron radiation facility (SSRF), China, where the X-ray wavelength is 0.6887 Å and the area detector is Pilatus3 2 M. The Bruker D8 Discover Diffractometer was used to perform X-ray reciprocal-space mapping (RSM). This diffractometer was equipped with a high-brilliance rotational Cu X-ray source, DUO detectors of the Scintillation counter, and LynxEye detector. The PZT/Nb: STO samples were measured in a grazing-incidence mode, with an exposure time of 5 s for each pattern. To extract thin-film lamellae from the bulk PZT/Nb: STO sample, an integrated Focused Ion Beam (FIB, Helios nanolab 600) and SEM (Hitachi S4700) were utilized. The Pt layer was deposited on the film surface to protect it from damage. Subsequent cross-sectional observations of the film were performed using a Transmission Electron microscope (TEM, FEI Tecnai G2 F20 S-TWIN) and an aberration-corrected transmission electron microscope (FEI Titan G2 80-200 Chemi STEM). The depth profiling of the ion signals throughout the films was characterized by Time-of-flight secondary ion mass spectra (TOF-SIMS, Iontof TOF.SIMS 5), with an experimental area of $200\ \mu m \times 200\ \mu m$. In the TOF-SIMS depth profiling, which was in positive polarity, a 30 keV primary-ion beam of $Bi_1^+$ first impacted the film surface, followed by a 2 keV sputtering beam of $O_2$.

### Polarization measurement

Both the oxygen octahedra and the Zr/Ti ions possess displacements from the center of the Pb ions within the tetragonal cell, which subsequently leads to the occurrence of spontaneous polarization. The displacements of Zr/Ti ions can serve as a means to determine the polarizations of PZT unit cells[20]. Consequently, the shifts of the Zr/Ti ions relative to the center of the four nearest Pb ion columns were quantified in cross-sectional HAADF-STEM-based images of extracted thin-film lamellae through the utilization of Digital Micrograph software.

### Electrical measurement

Measurements of dielectric, photovoltaic, and pyroelectric properties were completed with a capacitor structure with Ag (Pt) as the top electrode and Nb: STO substrates as the bottom electrode. Ag (Pt) electrodes (area: ~$0.00785\ cm^2$, thickness: ~40 nm) were deposited on the PTO or PZT surface by direct current (dc) sputtering (SD-3000). The frequency-dependent and temperature-dependent small-signal permittivity and the loss tangent were measured using a precision impedance analyzer (Agilent 4294A).

### Pyroelectric coefficient measurement

The stable pyroelectric current was measured using a Keithley 2636B electrometer test system in the heating or cooling process with a constant heating or cooling rate (±10 °C/min) between 20 and 30 °C. Pyroelectric coefficients analyzed by a dynamic method[13,37] can be calculated by

$$\pi = \frac{I_p}{A \times \frac{dT}{dt}} \tag{3}$$

where $\pi$ is the pyroelectric coefficient, $I_p$ is the pyroelectric current, $A$ is the area of electrode, $dT/dt$ is the rate of temperature change.

### Photovoltaic and pyroelectric measurement

Photovoltaic and pyroelectric properties of PZT films were collected using optical units from Thorlabs and source measure units (Keithley 2450). The samples were tested for photovoltaic current by illuminating with light from a continuous-wave 375-nm laser (MDL-III-375). To further illustrate the pyroelectric sensibility, a continuous-wave 1064-nm laser (MIL-III-1064) was chosen as the heat source to irradiate the samples. The current oscillations were achieved by switching the laser periodically on and off.

### Phase-field method

In the present work, the domain structure uses spontaneous polarization $P=(P_x,P_y,P_z)$ as the order parameter[38–43]. The temporal evolution of the polarization field is solved by the time-dependent Ginzburg–Landau (TDGL) equation:

$$\frac{\partial P_i(r,t)}{\partial t} = -L\frac{\delta F}{\delta P_i(r,t)}, i=x,y,z \tag{4}$$

where $r$ is the spatial coordinate, $t$ is the evolution time, $L$ is the kinetic coefficient that is related to the domain evolution. $F$ is the total free energy of the system, the thermodynamic driving force for polarization evolution. The total free energy of a bulk system can be defined as follows

$$F=\int_V [f_{\text{bulk}}+f_{\text{wall}}+f_{\text{elastic}}+f_{\text{elec}}]dV \tag{5}$$

Here, $F$ includes the bulk free energy density $f_{\text{bulk}}$, domain-wall energy density $f_{\text{wall}}$, elastic energy density $f_{\text{elastic}}$, and electrostatic energy density $f_{\text{elec}}$.

The bulk free-energy density is expressed for zero strain as a six-order polynomial expansion, that is

$$\begin{aligned} f_{\text{bulk}} = {} & \alpha_1\left(P_1^2+P_2^2+P_3^2\right)+\alpha_{11}\left(P_1^4+P_2^4+P_3^4\right)+\alpha_{12}\left(P_1^2P_2^2+P_2^2P_3^2+P_1^2P_3^2\right)+\alpha_{111}\left(P_1^6+P_2^6+P_3^6\right) \\ & +\alpha_{112}\left[P_1^4\left(P_2^2+P_3^2\right)+P_2^4\left(P_1^2+P_3^2\right)+P_3^4\left(P_1^2+P_2^2\right)\right]+\alpha_{123}P_1^2P_2^2P_3^2 \end{aligned} \tag{6}$$

where $\alpha_i$, $\alpha_{ij}$, and $\alpha_{ijk}$ are the Landau parameters that can be obtained from the experiment.

The specific expression of the elastic energy density is as follows

$$f_{\text{elastic}}=\frac{1}{2}C_{ijkl}(\varepsilon_{ij}-\varepsilon_{ij}^0)(\varepsilon_{kl}-\varepsilon_{kl}^0) \tag{7}$$

where $C_{ijkl}$ is the elastic stiffness tensor, $\varepsilon_{ij}$ is the total strain, and $\varepsilon_{ij}{}^o$ is the spontaneous strain during the phase transformation. The spontaneous strain is related to the polarization by the electrostrictive coefficients $\varepsilon_{ij}{}^o=Q_{ijkl}P_kP_l$, where $Q_{ijkl}$ is the electrostrictive coefficient.

The domain-wall energy density is written as

$$f_{\text{wall}}=\frac{1}{2}G_{ijkl}P_{i,j}P_{k,l} \tag{8}$$

where $G_{ijkl}$ is the gradient coefficient.

The electrostatic energy can be expressed as[44–46]

$$f_{\text{elec}}=-E_{appl}\,P-\frac{1}{2}E_{dipole}\,P \tag{9}$$

where $E_{\text{appl}}$ is the applied electric field, $E_{\text{dipole}}$ is the dipole-dipole interaction field. The potential is obtained through the electrostatic equilibrium equation[46].

For PZT[47], parameters in detail are provided as,

$$a_1=(T-T_0)/(2\omega_0C_0)\mathrm{C}^{-2}\mathrm{m}^2\mathrm{N} \tag{10}$$

$$a_{11}=(10.612-22.655x+10.955x^2)\times10^{13}/C_0\mathrm{C}^{-4}\mathrm{m}^6\mathrm{N} \tag{11}$$

$$a_{12}=\eta_1/3-a_{11}\mathrm{C}^{-4}\mathrm{m}^6\mathrm{N} \tag{12}$$

$$a_{111}=(12.026-17.296x+9.179x^2)\times10^{13}/C_0\mathrm{C}^{-6}\mathrm{m}^{10}\mathrm{N} \tag{13}$$

$$a_{112}=(4.2904-3.3754x+58.804e^{-29.397x})\times10^{14}/C_0\mathrm{C}^{-6}\mathrm{m}^{10}\mathrm{N} \tag{14}$$

$$a_{123}=\eta_2-3a_{111}-6a_{112}\mathrm{C}^{-6}\mathrm{m}^{10}\mathrm{N} \tag{15}$$

$$\eta_1=[2.6213+0.42743x-(9.6+0.012501x)e^{-12.6x}]\times10^{14}/C_0 \tag{16}$$

$$\eta_2=[0.887-0.76973x+(16.225-0.088651x)e^{-21.255x}]\times10^{15}/C_0 \tag{17}$$

When $0\le x\le0.5$,

$$C_0=\left[\frac{2.1716}{1+500.05(x-0.5)^2}+0.131x+2.01\right]\times10^5 \tag{18}$$

When $0.5<x\le1$,

$$C_0=\left[\frac{2.8339}{1+126.56(x-0.5)^2}+1.4132\right]\times10^5 \tag{19}$$

$x$ is the mole fraction of $PbTiO_3$ in PZT and $\omega_0$ is the dielectric permittivity of a vacuum. The electrostrictive coefficients[47] and elastic constants[48]:

$$Q_{11}=\frac{0.029578}{1+200(x-0.5)^2}+0.042796x+0.045624\ \mathrm{C}^{-2}\mathrm{m}^4 \tag{20}$$

$$Q_{12}=\frac{0.026568}{1+200(x+0.5)^2}-0.012093x-0.013386\ \mathrm{C}^{-2}\mathrm{m}^4 \tag{21}$$

$$Q_{44}=\frac{1}{2}\left[\frac{0.025325}{1+200(x-0.5)^2}+0.020857x+0.046147\right]\mathrm{C}^{-2}\mathrm{m}^4 \tag{22}$$

$s_{11}=8.0\times10^{-12}\ \mathrm{m^2N^{-1}}$, $s_{12}=-2.5\times10^{-12}\ \mathrm{m^2\ N^{-1}}$, $s_{44}=9.0\times10^{-12}\ \mathrm{m^2\ N^{-1}}$. The gradient energy coefficients[47] are $G_{11}/G_{110}=0.6$, $G_{12}/G_{110}=0$, $G_{44}/G_{110}=0.3$, where $G_{110}=1.73\times10^{-10}\ \mathrm{C^{-2}\ m^4\ N}$. The simulation scale is $64\times64\times64$, and the grid scales are 1 nm. We employed periodic boundary conditions. The semi-implicit Fourier-spectral method was used for solving the equations.

### Reporting summary

Further information on research design is available in the Nature Portfolio Reporting Summary linked to this article.

## Data availability

The data generated in this study are provided in the Supplementary Information/ Source Data files. Source data are provided with this paper.

## References

1. Dawber, M., Rabe, K. M. & Scott, J. F. Physics of thin-film ferroelectric oxides. *Rev. Mod. Phys.* **77**, 1083–1130 (2005).
2. Scott, J. F. Applications of modern ferroelectrics. *Science* **315**, 954–959 (2007).
3. Martin, L. W. & Rappe, A. M. Thin-film ferroelectric materials and their applications. *Nat. Rev. Mater.* **2**, 16087 (2016).

4. Pan, H. et al. Ultrahigh energy storage in superparaelectric relaxor ferroelectrics. *Science* **374**, 100–104 (2021).
5. Saito, Y. et al. Lead-free piezoceramics. *Nature* **432**, 84–87 (2004).
6. Li, F. et al. Giant piezoelectricity of Sm-doped Pb($Mg_{1/3}Nb_{2/3}$)$O_3$-$PbTiO_3$ single crystals. *Science* **364**, 264–268 (2019).
7. Agar, J. C. et al. Complex evolution of built-in potential in compositionally-graded $PbZr_{1-x}Ti_xO_3$ thin films. *ACS Nano* **9**, 7332–7342 (2015).
8. Zhang, Y. M. et al. Grain boundary diffusion hardening in potassium sodium niobate-based ceramics with full gradient composition and high piezoelectricity. *Adv. Funct. Mater.* **33**, 2306039 (2023).
9. Li, H., Bowen, C. R., Dan, H. & Yang, Y. Pyroelectricity induced by Schottky interface above the Curie temperature of bulk materials. *Joule* **8**, 401–415 (2024).
10. Choudhury, N., Walizer, L., Lisenkov, S. & Bellaiche, L. Geometric frustration in compositionally modulated ferroelectrics. *Nature* **470**, 513–517 (2011).
11. Mantese, J. V., Schubring, N. W., Micheli, A. L. & Catalan, A. B. Ferroelectric thin films with polarization gradients normal to the growth surface. *Appl. Phys. Lett.* **67**, 721–723 (1995).
12. Zhang, J., Xu, R., Damodaran, A. R., Chen, Z. H. & Martin, L. W. Understanding order in compositionally graded ferroelectrics: Flexoelectricity, gradient, and depolarization field effects. *Phys. Rev. B* **89**, 224101 (2014).
13. Meng, X. D., Huang, X. L., Zhi, W. H., Xing, B. H. & Tian, H. Dynamic of polar nanoregions and its impact on the pyroelectric and dielectric properties in paraelectric KTN materials. *J. Am. Ceram. Soc.* **106**, 3045–3051 (2023).
14. Zou, D. et al. Flexible and translucent PZT films enhanced by the compositionally graded heterostructure for human body monitoring. *Nano Energy* **85**, 105984 (2021).
15. Agar, J. C. et al. Highly mobile ferroelastic domain walls in compositionally graded ferroelectric thin films. *Nat. Mater.* **15**, 549–556 (2016).
16. Damodaran, A. R. et al. Large polarization gradients and temperature-stable responses in compositionally-graded ferroelectrics. *Nat. Commun.* **8**, 14961 (2017).
17. Zheng, T. et al. Compositionally graded KNN-based multilayer composite with excellent piezoelectric temperature stability. *Adv. Mater.* **34**, e2109175 (2022).
18. Vrejoiu, I. et al. Intrinsic ferroelectric properties of strained tetragonal $PbZr_{0.2}Ti_{0.8}O_3$ obtained on layer-by-layer grown, defect-free single-crystalline films. *Adv. Mater.* **18**, 1657–1661 (2006).
19. Mangalam, R. V., Agar, J. C., Damodaran, A. R., Karthik, J. & Martin, L. W. Improved pyroelectric figures of merit in compositionally graded $PbZr_{1-x}Ti_xO_3$ thin films. *ACS Appl. Mater. Interfaces* **5**, 13235–13241 (2013).
20. Tang, Y. L. et al. Observation of a periodic array offlux-closure quadrants in strainedferroelectric $PbTiO_3$ films. *Science* **348**, 547–551 (2015).
21. Ryu, J. et al. Upshift of phase transition temperature in nanostructured $PbTiO_3$ thick film for high temperature applications. *ACS Appl. Mater. Interfaces* **6**, 11980–11987 (2014).
22. Ren, Z. H. et al. Electrostatic force-driven oxide heteroepitaxy for interface control. *Adv. Mater.* **30**, e1707017 (2018).
23. Ohtomo, A., Muller, D. A., Grazul, J. L. & Hwang, H. Y. Artificial charge-modulationin atomic-scale perovskite titanate superlattices. *Nature* **419**, 378–380 (2002).
24. Lin, C. et al. Solution epitaxy of polarization-gradient ferroelectric oxide films with colossal photovoltaic current. *Nat. Commun.* **14**, 2341 (2023).
25. Mangalam, R. V., Karthik, J., Damodaran, A. R., Agar, J. C. & Martin, L. W. Unexpected crystal and domain structures and properties in compositionally graded $PbZr_{1-x}Ti_xO_3$ thin films. *Adv. Mater.* **25**, 1761–1767 (2013).
26. Talanov, M. V., Bush, A. A., Sirotinkin, V. P. & Kozlov, V. I. Structural origin of strongly diffused ferroelectric phase transition in Ba(Ti, Zr)$O_3$-based ceramics. *Acta Mater.* **227**, 117734 (2022).
27. Lencka, M. M., Anderko, A. & Riman, R. E. Hydrothermal precipitation of lead zirconate titanate solid solutions: thermodynamic modeling and experimental synthesis. *J. Am. Ceram. Soc.* **78**, 2609–2618 (1995).
28. Qiu, Z. C., Zhou, J. P., Zhu, G. Q., Liu, P. & Bian, X. B. Hydrothermal synthesis of Pb($Zr_{0.52}Ti_{0.48}$)$O_3$ powders at low temperature and low alkaline concentration. *Bull. Mater. Sci.* **32**, 193–197 (2009).
29. Karthik, J., Mangalam, R. V. K., Agar, J. C. & Martin, L. W. Large built-in electric fields due to flexoelectricity in compositionally graded ferroelectric thin films. *Phys. Rev. B* **87**, 024111 (2013).
30. Lupi, E. et al. Large polarization and susceptibilities in artificial morphotropic phase boundary $PbZr_{1-x}Ti_xO_3$ superlattices. *Adv. Electron Mater.* **6**, 1901395 (2020).
31. Zhu, C. et al. High temperature lead-free BNT-based ceramics with stable energy storage and delectric properties. *J. Mater. Chem. A* **8**, 683–692 (2020).
32. Ding, Y. et al. High capacitive performance at moderate operating field in ($Bi_{0.5}Na_{0.5}$)$TiO_3$-based dielectric ceramics via synergistic effect of site engineering strategy. *Chem. Eng. J.* **426**, 130811 (2021).
33. Yang, G. et al. Giant dielectric response and relaxation behavior of $Bi^{3+}/W^{6+}$ co-doped $TiO_2$ ceramics. *Phys. Chem. Chem. Phys.* **26**, 8834–8841 (2024).
34. Taylor, D. V. & Damjanovic, D. Domain wall pinning contribution to the nonlinear dielectric permittivity in Pb(Zr, Ti)$O_3$ thin films. *Appl. Phys. Lett.* **73**, 2045–2047 (1998).
35. Fujii, I. & Trolier-McKinstry, S. Temperature dependence of dielectric nonlinearity of $BaTiO_3$ ceramics. *Microstructures* **3**, 2023045 (2023).
36. Sebald, G., Lefeuvre, E. & Guyomar, D. Pyroelectric energy conversion: optimization principles. *IEEE Trans. Ultrason. Ferroelectr. Freq. Control* **55**, 538–551 (2008).
37. Daglish, M. A dynamic method for determining the pyroelectric response of thin films. *Integr. Ferroelectr.* **22**, 473–488 (1998).
38. Liu, D. et al. Phase-field simulations of vortex chirality manipulation in ferroelectric thin films. *npj Quantum Mater.* **7**, 34 (2022).
39. Xu, S. Q. et al. Strain engineering of energy storage performance in relaxor ferroelectric thin film capacitors. *Adv. Theor. Simul.* **5**, 2100324 (2022).
40. Gao, R. Z., Shi, X. M., Wang, J. & Huang, H. B. Understanding electrocaloric cooling of ferroelectrics guided by phase-field modeling. *J. Am. Ceram. Soc.* **105**, 3689–3714 (2022).
41. Shao, C. C., Shi, X. M., Wang, J., Xu, J. W. & Huang, H. B. Designing ultrafast cooling rate for room temperature electrocaloric effects by phase-field simulations. *Adv. Theor. Simul.* **5**, 2200406 (2022).
42. Ren, J., Tang, S. Y., Guo, C. Q., Wang, J. & Huang, H. B. Surface effect of thickness-dependent polarization and domain evolution in $BiFeO_3$ epitaxial ultrathin films. *ACS Appl. Mater. Interfaces* **16**, 1074–1081 (2023).
43. Xu, K., Shi, X. M., Dong, S. Z., Wang, J. & Huang, H. B. Antiferroelectric phase diagram enhancing energy-storage performance by phase-field simulations. *ACS Appl. Mater. Interfaces* **14**, 25770–25780 (2022).
44. Shu, W. L., Wang, J. & Zhang, T. Y. Effect of grain boundary on the electromechanical response of ferroelectric polycrystals. *J. Appl. Phys.* **112**, 064108 (2012).
45. Wang, J. J., Wang, B. & Chen, L. Q. Understanding, predicting, and designing ferroelectric domain structures and switching guided by the phase-field method. *Ann. Rev. Mater. Res.* **49**, 127–152 (2019).
46. Li, Y. L. et al. Ferroelectric domain structures in $SrBi_2Nb_2O_9$ epitaxial thin films: Electron microscopy and phase-field simulations. *J. Appl. Phys.* **95**, 6332–6340 (2004).

47. Pertsev, N. A. et al. Effect of mechanical boundary conditions on phase diagrams of epitaxial ferroelectric thin films. *Phys. Rev. Lett.* **80**, 1988–1991 (1998).
48. Xu, G. Y., Zhong, Z., Bing, Y., Ye, Z. G. & Shirane, G. Electric-field-induced redistribution of polar nano-regions in a relaxor ferroelectric. *Nat. Mater.* **5**, 134–140 (2006).

## Acknowledgements

Z.R. (ZJU), H.T., and G.H. acknowledge financial support from National Key R&D Program of China (Grant No. 2021YFA1500800), the National Natural Science Foundation of China (Grant No. 52272129 and No. 12125407), Joint Funds of the National Natural Science Foundation of China (Grant No. U21A2067), the Zhejiang Provincial Natural Science Foundation (Grant No. LR21E020004), and the Shanxi-Zheda Institute of Advanced Materials and Chemical Engineering (Grant No. 2021SZ-FR007). We thank the beamline 17B1 of the National Centre for Protein Science Shanghai at Shanghai Synchrotron Radiation Facility (SSRF) for the help in GIWAXS characterizations. C.L. acknowledges financial support from the Zhejiang Provincial Key R&D Program of China (Grant No. 2021C01026 and 2021C05002), and the Leading Innovative and Entrepreneur Team Introduction Program of Zhejiang (Grant No. 2020R01007). Z.Z. acknowledges financial support from the Postdoctoral Fellowship Program of CPSF (Grant No. GZB20240667) and Priority-Funded Postdoctoral Research Project, Zhejiang Province (Grant No. ZJ2024002). Q.Z. acknowledges financial support from the Shanghai Key Laboratory of Material Frontiers Research in Extreme Environments, China (Grant No. 22dz2260800) and the Shanghai Science and Technology Committee, China (Grant No. 22JC1410300).

## Author contributions

Z.R. (ZJU) and G.H. initiated the work. Z.R. (ZJU), G.H., H.T., H.H.(BIT), and Q.Z. designed the experiments and calculations and supervised the analysis of obtained results. R.Z., C.L., and Y.S. (ZJU) synthesized the samples and conducted the macroscopic morphology and structure characterization. Z.Z. and H.T. completed the TEM studies, analyzed the TEM data, and measured the polarization. H.H. (THU), Y.W. (THU), J.M., and Y.W. (ZJU) conducted permittivity measurements. Y.S. (BIT) and H.H. (BIT) performed the calculations. Z.R. (IHEP), H.D., X.M., and Q.Z. conducted the synchrotron radiation XRD experiments and the analysis. H.D. performed the X-ray RSM and TOF-SIMS experiments and the analysis. R.Z. and C.L. carried out the photovoltaic and pyroelectric measurements and contributed to the growth model for composition gradient. R.Z., C.L., H.D., and Z.R. (ZJU) contributed to the analysis and understanding of the data and co-wrote the manuscript. Z.R. (ZJU), H.H. (BIT), Q.Z., H.T., and G.H. revised the manuscript. All authors participated in the analysis and discussion.

## Competing interests

The authors declare no competing interests.

## Additional information

**Supplementary information** The online version contains supplementary material available at https://doi.org/10.1038/s41467-024-55411-7.

**Correspondence** and requests for materials should be addressed to Qiaoshi Zeng, He Tian, Zhaohui Ren or Gaorong Han.

**Peer review information** *Nature Communications* thanks Abdolhamid Akbarzadeh Shafaroudi, Gyaneshwar Sharma and the other anonymous reviewer(s) for their contribution to the peer review of this work. A peer review file is available.